

## Low-loss arrayed waveguide grating at 760 nm

E. J. STANTON,\* A. SPOTT, M. L. DAVENPORT, N. VOLET, AND J. E. BOWERS

Department of Electrical and Computer Engineering, University of California, Santa Barbara, California 93106, USA

\*Corresponding author: estanton@ece.ucsb.edu

Received 24 February 2016; accepted 12 March 2016; posted 17 March 2016 (Doc. ID 258264); published 11 April 2016

**An arrayed waveguide grating (AWG) at 760 nm is demonstrated with an insertion loss smaller than 0.5 dB. Interface roughness and waveguide length errors contribute much more to scattering loss and phase errors at 760 nm than at longer wavelengths, thus requiring improved design and fabrication. This Letter details how this is achieved by minimizing interfacial scattering, grating side-order excitation, and phase errors in the AWG. With silicon nitride core and silicon dioxide clad waveguides on silicon, this AWG is compatible with heterogeneously integrated lasers for on-chip spectral beam combining.** © 2016 Optical Society of America

**OCIS codes:** (060.4230) Multiplexing; (130.7408) Wavelength filtering devices; (140.3298) Laser beam combining.

<http://dx.doi.org/10.1364/OL.41.001785>

Spectral beam combiners with heterogeneously integrated lasers would enable many applications in need of either high-power and broadband or coherent and multiplexed light sources [1,2]. In particular, an integrated multi-spectral source near the visible is compelling for spectroscopy [3] or as a wavelength-division multiplexing (WDM) high brightness source for free-space communications [4]. An arrayed waveguide grating (AWG) can efficiently combine light sources of closely spaced wavelengths and is a key component for broadband spectral beam combiners [1].

AWGs at visible wavelengths have yet to be demonstrated with less than 5.0 dB insertion loss [5,6]. One demonstration at 890 nm shows 1.2 dB insertion loss [7]. However, even lower loss is desired for most applications, and more than 1 dB of loss is prohibitive for power scaling. The main challenges involved in making high-performance AWGs at visible wavelengths stem from interfacial scattering and phase errors due to waveguide length errors. The former is similar to Rayleigh scattering with a  $1/\lambda^4$  dependence, and the latter scales with a  $1/\lambda$  dependence of the waveguide propagation constant. Many high-performance AWGs have previously been demonstrated in the near-infrared [8–10], leveraging on significantly smaller interfacial scattering and phase errors, compared to visible AWGs. A low insertion loss AWG near visible must combine techniques to achieve state-of-the-art sidewall roughness and material absorption, low side-order grating excitation at the input and output free propagation regions (FPRs), low loss from waveguide bends, and low phase errors in the arrayed waveguides.

Ultra-low-loss silicon nitride ( $\text{Si}_3\text{N}_4$ ) core and silicon dioxide ( $\text{SiO}_2$ ) clad waveguides have been demonstrated by minimizing interfacial scattering loss [11] or minimizing material absorption [12]. In addition, phase errors due to grid snapping during the mask writing process, as shown in [13,14], can be reduced by using the smallest possible address unit. These two techniques previously demonstrated in AWG designs are used in this Letter. In addition, we use a new AWG design technique based on simulated waveguide modes and a numerical far-field calculation, instead of the Gaussian-shaped mode approximation that is usually used [15]. This provides an accurate model for the transmission spectra, including insertion loss and non-uniformity, while reducing the computation time. In addition, we incorporate adiabatic waveguide bend transitions so each arrayed waveguide can have identical bends without introducing loss due to mode mismatch between straight and curved sections. This prevents phase errors from varying bend modes between arrayed waveguides.

The challenges preventing previous demonstrations of near-visible AWGs from achieving low insertion loss have been addressed in this Letter by eliminating bend mode mismatch, using high aspect ratio waveguides, minimizing the mask address unit, and optimizing the fabrication process with photoresist re-flow to reduce interfacial roughness and high temperature baking to reduce hydrogen impurities. Using  $\text{Si}_3\text{N}_4$  core and  $\text{SiO}_2$  clad waveguides on Si provides a suitable platform for this low-loss 760 nm AWG. It is compatible with heterogeneously integrated lasers [16] and, therefore, enables technologies that integrate lasers and spectral beam combiners at the near visible. In this Letter, we describe the AWG design and performance. In particular, an insertion loss smaller than 0.5 dB for the best channel case and a crosstalk below 23 dB are demonstrated.

This AWG is designed with a center wavelength of 760 nm and eight channels spectrally separated by 0.5 nm. The waveguide core geometry is 60 nm thick and 1.0  $\mu\text{m}$  wide and laterally tapers to 1.6  $\mu\text{m}$  width at the FPR interfaces. The Rowland radius is 180  $\mu\text{m}$ . Forty-seven arrayed waveguides are separated by at least 3  $\mu\text{m}$  in the array and 0.4  $\mu\text{m}$  at the FPR interface. There are two identical bends for each arrayed waveguide to minimize phase errors from varying bend modes between waveguides, as shown in Fig. 1. This configuration is typically avoided because two additional straight-to-bend junctions are necessary, compared to the configuration with a single bend in each arm [15]. However, the bends in our design feature tapered bend

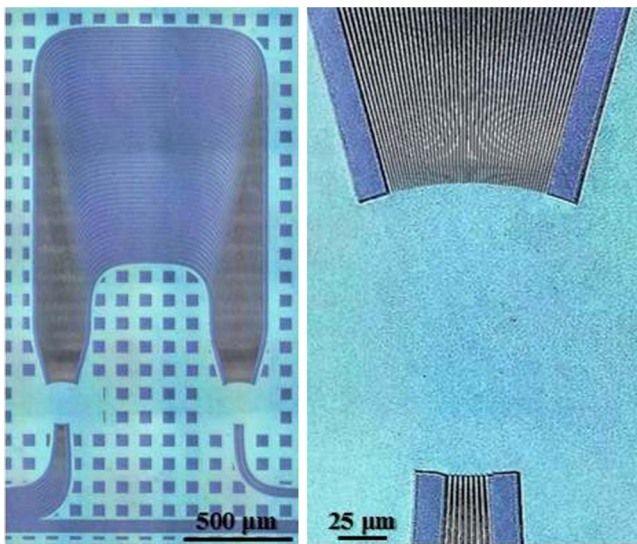


**Fig. 1.** Micrographs (left) of the free propagation region interface and (right) of the full AWG.

radii to minimize this junction loss. Each  $90^\circ$  bend is divided into 25 segments of varying radii to create an adiabatic transition between straight and curved sections of the waveguide, which have a minimum radius of  $150 \mu\text{m}$ . The AWG is designed for TE polarization operation, which is compatible with integrated diode lasers, so TM polarized transmission is not investigated. The total footprint of the AWG is  $2.8 \text{ mm}^2$ .

Excitation of side-order grating modes in the FPRs is minimized by increasing the density of arrayed waveguides at the FPR interfaces and by decreasing the far-field divergence of each grating element [17]. We define the waveguide density as the center-to-center waveguide spacing. Two parameters affect this waveguide density. First, minimizing the waveguide separation while maintaining the waveguide width increases the density without affecting the far-field profile of the array if the waveguide mode is not significantly perturbed by the adjacent waveguides. However, the minimum waveguide separation is limited by fabrication processes. Second, decreasing the waveguide width while maintaining the waveguide separation increases the density, but also dictates the far-field profile. Figure 2 shows the simulated far-field divergence of the  $\text{TE}_{00}$  waveguide mode into the FPR. It also shows the effective refractive indices for the first three TE modes. Increasing the waveguide width decreases the far-field divergence for widths greater than  $0.8 \mu\text{m}$ , at the expense of waveguide density. It also begins to support higher-order TE modes which collect some of the light, introducing loss and phase errors. Narrowing the far-field divergence may reduce the side-order excitation and, consequently, the center-channel insertion loss, but it also increases the nonuniformity. The fabricated design we demonstrate here uses  $1.6 \mu\text{m}$  wide waveguides at the FPR interface to compromise these loss mechanisms. Future work is planned to develop a technique to quantify these loss contributions and optimize the waveguide width and height.

Phase errors in the AWG can be reduced by using the smallest possible address unit and minimizing the interfacial scattering, especially from the waveguide sidewall. This can also be achieved by designing the waveguides with a small value for  $\partial\beta/\partial w$ , where  $\beta$  is the waveguide propagation constant and

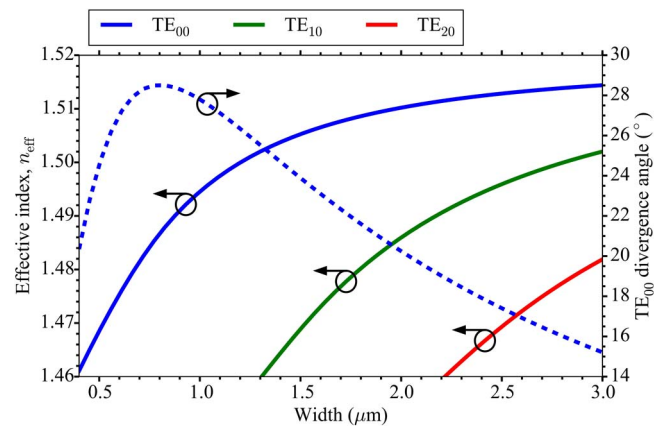


**Fig. 2.** Effective index calculated for the first three TE modes as a function of the waveguide width and divergence angle of  $\text{TE}_{00}$  into the slab mode of the free propagation region.

$w$  is the waveguide width [18]. For this design, a  $5 \text{ nm}$  address unit is used. However, a smaller address unit is desired, if possible, but this was the smallest address unit available to us. From Fig. 2,  $\partial\beta/\partial w$  is determined to be  $0.3 \text{ rad}/\mu\text{m}^2$  for the fundamental  $\text{TE}_{00}$  mode of a  $1.0 \mu\text{m}$  wide and  $60 \text{ nm}$  thick arrayed waveguide. Scattering loss is minimized by optimizing the lithography and etching processes to reduce the waveguide's sidewall roughness and by maximizing the waveguide width-to-height ratio for a desired minimum bend radius, as discussed in [11].

Fabrication begins with  $100 \text{ mm}$  Si wafers and growing  $2 \mu\text{m}$  of thermal  $\text{SiO}_2$ . Sixty nm of  $\text{Si}_3\text{N}_4$  are deposited on both sides of the wafer by low-pressure chemical vapor deposition (LPCVD). Deep UV lithography with Shipley AR2 anti-reflectant and MicroChem UV6 photoresist defines the AWG pattern. After developing the resist, it is re-flowed at  $135^\circ\text{C}$  for  $30 \text{ s}$  to create a smooth pattern for etching the waveguides with  $\text{CF}_4/\text{CHF}_3/\text{O}_2$  inductively coupled plasma (ICP). A  $2 \mu\text{m}$  thick  $\text{SiO}_2$  top cladding is deposited with plasma enhanced chemical vapor deposition (PECVD). The wafer is then diced, and the facets are mechanically polished.

The waveguide sidewall and surface roughness are measured with an atomic force microscope (AFM) before the top oxide deposition, as shown in Fig. 3. The sidewall roughness is assumed to be nonisotropic, with a correlated roughness in the direction of the etch [18], while the surface roughness is isotropic, as expected. By measuring the sidewall position deviation and the height deviation at the center of the waveguide, two one-dimensional (1D) scans are generated to calculate the sidewall and top surface roughness parameters. The auto-covariance function is applied to each scan, and an exponential fit [19] is used to calculate the standard deviations  $\sigma_{\text{side}} = 1.4 \text{ nm}$  and  $\sigma_{\text{surface}} = 0.7 \text{ nm}$  and correlation lengths  $L_{\text{c,side}} = 51.0 \text{ nm}$  and  $L_{\text{c,surface}} = 89.7 \text{ nm}$ . Figures 3(a) and 3(b) show the AFM scans of the waveguide sidewall and top surface. Figures 3(c) and 3(d) show the corresponding 1D scan data and auto-covariance functions of the scans with exponential fits.

To ensure low insertion loss, total propagation loss is estimated by calculating the bend mode radiation and interfacial scattering as a function of curvature, corresponding to each  $90^\circ$  bend of the arrayed waveguides. Bend modes and radiation losses are calculated with FIMMWAVE [20], and the interfacial scattering losses are calculated as in [19,21], using the measured

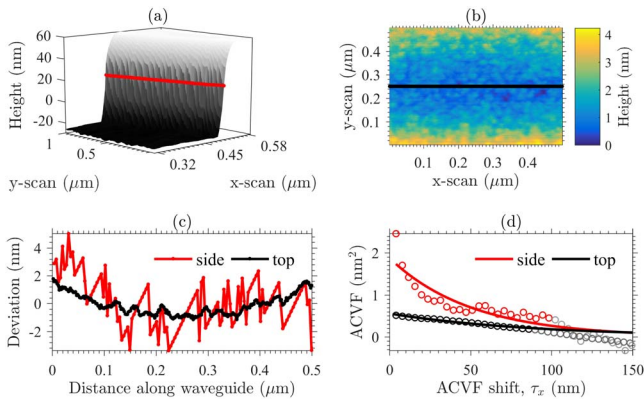


**Fig. 3.** (a) AFM scan of waveguide sidewall and a red line indicating the data points used in (c). (b) AFM scan of the top surface of the waveguide and a black line indicating the data points used in (c). (c) Sidewall position deviation of the waveguide at 20 nm height (red line) and the waveguide-center height deviation (black line), both along the waveguide propagation direction. (d) Auto-covariance function (ACVF) of the AFM scans in (c) for both sidewall and top surface shown in red and black circles, respectively, with the uncorrelated data points shown in gray. The exponential fits to sidewall and top surface ACVF are shown in red and black solid lines. The gray uncorrelated data points are not used in the fit since they tend to negative values, while the fitting exponential function is strictly positive.

sidewall and surface roughness parameters. The results of these calculations are shown in Fig. 4. The minimum bend radius of 150  $\mu\text{m}$ , corresponding to the maximum curvature of  $6.67 \text{ mm}^{-1}$ , has negligible radiation loss on the order of 0.05 dB/m.

It is reported in [12] that the dominating absorption loss mechanism is due to bond resonances from hydrogen impurities. In that report, the measured absorption resonances near 1540 nm are second-order resonances, so the first-order resonances are expected to occur near 770 nm. We do not have a method to measure the first-order bond resonance absorption peaks directly. Regardless, the fabrication process for this AWG is designed to reduce hydrogen impurities by baking the wafers at 1050°C for 10 h before and after the top  $\text{SiO}_2$  deposition. Therefore, since absorption loss is not included, the combined bend radiation and interfacial scattering loss of 21 dB/m in Fig. 4 predicts the minimum limit of the total propagation loss.

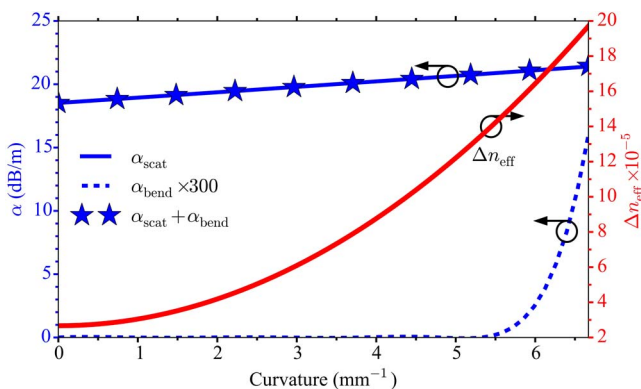


**Fig. 4.** Simulation of scattering loss  $\alpha_{\text{scat}}$ , bend loss  $\alpha_{\text{bend}}$ , and change  $\Delta n_{\text{eff}}$  in effective refractive index versus curvature.

The AWG transmission spectra are measured with a tunable laser and an optical spectrum analyzer (OSA). The tunable laser free space output beam is coupled through an isolator with an isolation  $>25$  dB. It is then coupled into an anti-reflection (AR)-coated polarization maintaining (PM) fiber with an AR-coated aspheric lens, both with  $<0.5\%$  reflection. The output facet of the PM fiber is connected to a three-axis piezo-controlled input coupling stage, which holds a compact setup with an AR-coated collimating lens, a linear polarizer with a 45 dB extinction ratio aligned with the on-chip TE polarization, and an AR-coated objective lens to focus the light to the AWG input facet. The collimating lens, the polarizer, and the objective lens are aligned to each other, and their collective position is controlled by one three-axis stage. The AWG chip is mounted on a fixed stage, and a lensed fiber is aligned to the output facet with another three-axis piezo-controlled stage, which is then connected to the OSA. The peak lasing wavelength is detected by the OSA as the laser wavelength is tuned, and a 0.3 nm span centered at the lasing wavelength is integrated for each data point in the AWG transmission spectra. Using the OSA instead of a photodiode reduces side-mode noise caused by the side-mode suppression ratio of the laser, which is measured to be  $30 \pm 4$  dB across the tuning range of 757–763 nm.

Figure 5 shows the measured and theoretical transmission spectra of the AWG, which are in good agreement. Calculations for the theoretical transmission spectra include sources of phase error, as described in [22] Eq. (5), from the measured roughness and the mask address unit. The phase error is calculated from Eq. (A2) in [18], where the shortest waveguide is 1.47 mm long and the length increment is 51.16  $\mu\text{m}$ . The waveguide size error is modeled by a normal distribution with standard deviation from the AFM data. The length error is modeled by a pseudo-random distribution between  $\pm 15$  nm of length in the arrayed waveguides, corresponding to a phase error of  $\pm \pi/16$  radians, similar to the calculation described in [13].

The transmission spectrum of each channel is normalized to one of a straight waveguide with the same facet geometry. From the normalized transmission spectrum, the worst-case single channel crosstalk is 23 dB, and the center channel insertion loss is 0.1 dB at the peak of the fifth channel, shown in yellow. The nonuniformity is 1.7 dB, and the free spectral range is 6.9 nm. The fourth channel, shown in green, exhibits uniformly lower transmission, which is likely due to an undesired

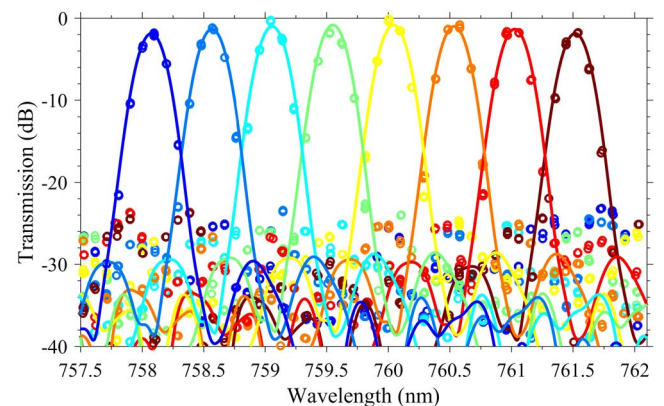


**Fig. 5.** Normalized measured transmission spectra (circles) of the AWG, compared with theory (solid lines). Each of the eight channels is represented by a different color.

particle scattering light near the demultiplexed waveguide associated with that channel. The theoretical AWG transmission spectra use an adjusted modal refractive index, which deviates from the simulated value by 3.4%. These calculated transmission spectra predict an insertion loss of 0.83 dB and a nonuniformity of 1.04 dB. This insertion loss comes from side-order excitation of 0.59 dB, the limited aperture of arrayed waveguides contributing 0.09 dB loss, predicted propagation loss of 0.10 dB, and the phase error from the sidewall roughness and length error contributing 0.05 dB loss. The most probable reason for the discrepancy between measured and theoretical insertion loss is that the actual far-field profile from the arrayed waveguides is narrower than the simulated one due to perturbation from the adjacent waveguides. This would decrease the side-order excitation, resulting in lower insertion loss of the central channel, and increase the nonuniformity of the experimental results compared to the theoretical calculations.

In conclusion, an AWG centered at 760 nm is demonstrated with an insertion loss smaller than 0.5 dB for the best channel case and a crosstalk below 23 dB. This proves the feasibility of integrated spectral beam combiners at near-visible wavelengths. Low insertion loss is achieved by minimizing side-order grating excitation, interfacial scattering, material absorption, and multiple sources of phase errors in the AWG. Integrated technologies for sensing, WDM communication, and high brightness broadband sources at these wavelengths are now feasible. Furthermore, these same techniques can be applied to AWG design to achieve low loss, enabling beam combining technologies at other wavelengths.

**Funding.** Office of Naval Research (ONR) (N00014-13-C-0147); National Science Foundation (NSF) (DGE 1144085); Schweizerischer Nationalfonds zur Förderung der Wissenschaftlichen Forschung (SNF).

**Acknowledgment.** The authors thank the Nanotech Facility at UCSB and Jared F. Bauters at Aurion, Inc., for helpful discussions.

## REFERENCES

1. E. J. Stanton, M. J. R. Heck, J. Bovington, A. Spott, and J. E. Bowers, *Opt. Express* **23**, 11272 (2015).

2. G. Roelkens, U. Dave, A. Gassenq, N. Hattasan, C. Hu, B. Kuyken, F. Leo, A. Malik, M. Muneeb, E. Ryckeboer, D. Sanchez, S. Uvin, R. Wang, Z. Hens, R. Baets, Y. Shimura, F. Gencarelli, B. Vincent, R. Loo, J. Van Campenhout, L. Cerutti, J.-B. Rodriguez, E. Tournie, X. Chen, M. Nedeljkovic, G. Mashanovich, L. Shen, N. Healy, A. Peacock, X. Liu, R. Osgood, and W. Green, *IEEE J. Sel. Top. Quantum Electron.* **20**, 394 (2014).
3. Z. Hu, A. Glidle, C. N. Ironside, M. Sorel, M. J. Strain, J. Cooper, and H. Yin, *Lab Chip* **12**, 2850 (2012).
4. S. Bloom, E. Korevaar, J. Schuster, and H. Willebrand, *J. Opt. Netw.* **2**, 178 (2003).
5. Y. Komai, H. Nagano, K. Okamoto, and K. Kodate, *Jpn. J. Appl. Phys.* **45**, 6742 (2006).
6. B. Schauwecker, G. Przyrembel, B. Kuhlow, and C. Radehaus, *IEEE Photon. Technol. Lett.* **12**, 1645 (2000).
7. D. Martens, A. Subramanian, S. Pathak, M. Vanslebrouck, P. Bienstman, W. Bogaerts, and R. Baets, *IEEE Photon. Technol. Lett.* **27**, 137 (2015).
8. A. Sugita, A. Kaneko, K. Okamoto, M. Itoh, A. Himeno, and Y. Ohmori, *IEEE Photon. Technol. Lett.* **12**, 1180 (2000).
9. D. Dai, Z. Wang, J. F. Bauters, M.-C. Tien, M. J. R. Heck, D. J. Blumenthal, and J. E. Bowers, *Opt. Express* **19**, 14130 (2011).
10. J. F. Bauters, J. R. Adleman, M. J. R. Heck, and J. E. Bowers, *Appl. Phys. A* **116**, 427 (2014).
11. J. F. Bauters, M. J. R. Heck, D. John, D. Dai, M.-C. Tien, J. S. Barton, A. Leinse, R. G. Heideman, D. J. Blumenthal, and J. E. Bowers, *Opt. Express* **19**, 3163 (2011).
12. J. F. Bauters, M. J. R. Heck, D. D. John, J. S. Barton, C. M. Bruinink, A. Leinse, R. G. Heideman, D. J. Blumenthal, and J. E. Bowers, *Opt. Express* **19**, 24090 (2011).
13. S. Pathak, M. Vanslebrouck, P. Dumon, D. Van Thourhout, P. Verheyen, G. Lepage, P. Absil, and W. Bogaerts, *IEEE Photon. Technol. Lett.* **26**, 718 (2014).
14. C. D. Lee, W. Chen, Q. Wang, Y.-J. Chen, W. T. Beard, D. Stone, R. F. Smith, R. Mincher, and I. R. Stewart, *J. Lightwave Technol.* **19**, 1726 (2001).
15. M. Smit and C. Van Dam, *IEEE J. Sel. Top. Quantum Electron.* **2**, 236 (1996).
16. J. T. Bovington, M. J. R. Heck, and J. E. Bowers, *Opt. Lett.* **39**, 6017 (2014).
17. S. Pathak, D. V. Thourhout, and W. Bogaerts, *Opt. Lett.* **38**, 2961 (2013).
18. T. Goh, S. Suzuki, and A. Sugita, *J. Lightwave Technol.* **15**, 2107 (1997).
19. T. Barwicz and H. Haus, *J. Lightwave Technol.* **23**, 2719 (2005).
20. [www.photon.com](http://www.photon.com).
21. C. Ciminelli, V. Passaro, F. Dell'Olio, and M. Armenise, *J. Eur. Opt. Soc.* **4**, 09015 (2009).
22. J. K. Hsiao, *Radio Sci.* **19**, 292 (1984).